The December 6, 2025 M_w7.0 earthquake in Yukon, Canada: Tectonic significance and observations of ground failure

*Theron Finley**
Yukon Geological Survey

Jeremy M. Gosselin
Natural Resources Canada, Geological Survey of Canada–Pacific

Katherine M. Biegel
Earth and Planetary Sciences, University of California Davis

Panya S. Lipovsky and Derek C. Cronmiller
Yukon Geological Survey

Andrew J. Schaeffer
Natural Resources Canada, Geological Survey of Canada–Pacific

Jan Dettmer
Yukon Geological Survey

Finley, T., Gosselin, J.M., Biegel, K.M., Lipovsky, P.S., Cronmiller, D.C., Schaeffer, A.J. and Dettmer, J., 2026. The December 6, 2025 M_w7.0 earthquake in Yukon, Canada: Tectonic significance and observations of ground failure. *In*: Yukon Exploration and Geology 2025, A. Stuart, L.H. Weston and S.K. Schultz (eds.), Yukon Geological Survey, Government of Yukon, p. 131–148.

Abstract

The December 6, 2025 moment magnitude (M_w) 7.0 earthquake in southwestern Yukon was the largest onshore earthquake in Canada in over 75 years. It caused no casualties or damage to the built environment but offers insight into the complex active tectonics of the St. Elias orogen and hazards posed by major faults in the Yukon. It also caused widespread landslides and avalanche activity, providing an opportunity to study relationships between ground shaking and mass wasting. Here, we use double-difference relocation to refine the location of the mainshock and 3280 ensuing aftershocks. Based on satellite imagery and a reconnaissance flight to the epicentral area, we compile a preliminary inventory of over 200 landslides and other surface effects caused by the event. During the December 12, 2025 flight, no evidence of a surface rupture was observed. The areal extent of landslide occurrences was also considerably smaller than expected based on empirical data from past earthquakes, possibly due to the cold temperatures and presence of permafrost. The earthquake relocations and landslide distribution indicate that the main rupture and strongest shaking occurred beneath the Mt. King George massif. We infer that the rupture occurred on the southernmost section of the hypothesized Totschunda-Fairweather Connector fault. Slip initiated with strike-slip motion, rupturing northwestward, and may have activated a conjugate reverse fault toward the northwest segment of the rupture.

* theron.finley@yukon.ca

Plain language summary

On December 6, 2025 a major earthquake occurred in southwestern Yukon, near Mt. Logan (Canada's tallest peak) in the St. Elias Mountains. The earthquake had a magnitude of 7.0 and was the largest to have occurred beneath the Canadian landmass since 1946 (there have been larger earthquakes more recently, but these have been beneath the ocean). Thankfully, there were no deaths or injuries caused by the earthquake, and no damage to roads or buildings. Due to its shallow depth and location beneath mountainous terrain, the earthquake caused many landslides and avalanches. By studying this earthquake, we can learn more about ongoing tectonic activity in the St. Elias mountain range, which is complex and one of the most rapidly deforming regions on earth. We can also gain knowledge about the relationships between earthquakes and landslides. This information will help to better understand the risks that earthquakes and landslides pose to Yukon communities. In this paper we provide more accurate earthquake locations than were initially available following the earthquake. These give us a better idea of the location and orientation of the fault that broke in this earthquake. We also provide photos and observations of landslides from a helicopter flight we took to the site of the earthquake. Our more accurate earthquake locations, as well as the distribution of landslides, suggests that the earthquake mostly occurred beneath Mt. King George. It has long been theorized that a fault referred to as the Connector fault exists in this region, but it has been difficult to prove given the remoteness of the area and the heavily glaciated terrain. Our results provide strong evidence for the existence of the Connector fault.

Introduction

On December 6, 2025, a moment magnitude (M_w) 7.0 earthquake occurred in the remote icefields of southwest Yukon, beneath Mt. King George and the Hubbard Glacier in the St. Elias Mountains (Fig. 1). The earthquake occurred within Kluane National Park and the Traditional Territory of the Kluane First Nation. Though the area in the vicinity of the event is uninhabited, shaking was reported in many nearby Yukon communities, including throughout Whitehorse (Natural Resources Canada, 2025). This event was among the largest instrumentally recorded earthquakes in Canadian history, and the largest onshore/crustal event since 1946 (Cassidy et al., 2010). The rupture was shallow (<10 km) and consequently triggered extensive landslides and avalanches in the mountainous epicentral area, providing an excellent opportunity to study relationships between shaking and mass wasting. Moreover, the event is tectonically significant as it provides evidence of the hypothesized Fairweather-Totschunda Connector fault (CF) that serves as a structural link and mechanism for strain transfer within the St. Elias orogen, and which has been hypothesized for decades (e.g., Richter and Matson, 1971).

We provide an overview of the seismicity and ground failure associated with this event. We use double-difference relocation (Waldhauser and Ellsworth, 2000) to improve the relative precision of hypocentral locations of the mainshock and aftershocks. Analysis of the relocated events, combined with available moment tensor (MT) solutions, offer insights into the geometry and kinematics of the structures that hosted the recent earthquake sequence. Furthermore, we compile a preliminary landslide inventory based on satellite imagery and a reconnaissance flight to the area. Our results have implications for the understanding of neotectonics and natural hazards in the Yukon.

Background

Tectonic setting

The current tectonic setting of southwestern Yukon is primarily governed by the ongoing oblique collision of the Yakutat microplate (a thick and buoyant oceanic plateau), and its shallow subduction beneath North America (Fig. 1; Eberhart-Phillips et al., 2006; Christeson et al., 2010; Pavlis et al., 2019). Within this broader plate-boundary framework, deformation is especially concentrated in the St. Elias Mountains, where oblique convergence at the northeastern corner of the plate margin has driven rapid uplift and exhumation over the last 36 Ma (Finzel et al., 2011), producing one of the most rapidly deforming orogenic systems on Earth (Enkelmann et al., 2008). The active deformation is the cause for numerous major earthquakes observed in the region over the past 100+ years (Fig. 1). The Yakutat microplate remains mechanically coupled to the Pacific plate, which translates northward along the Queen Charlotte–Fairweather transform fault system

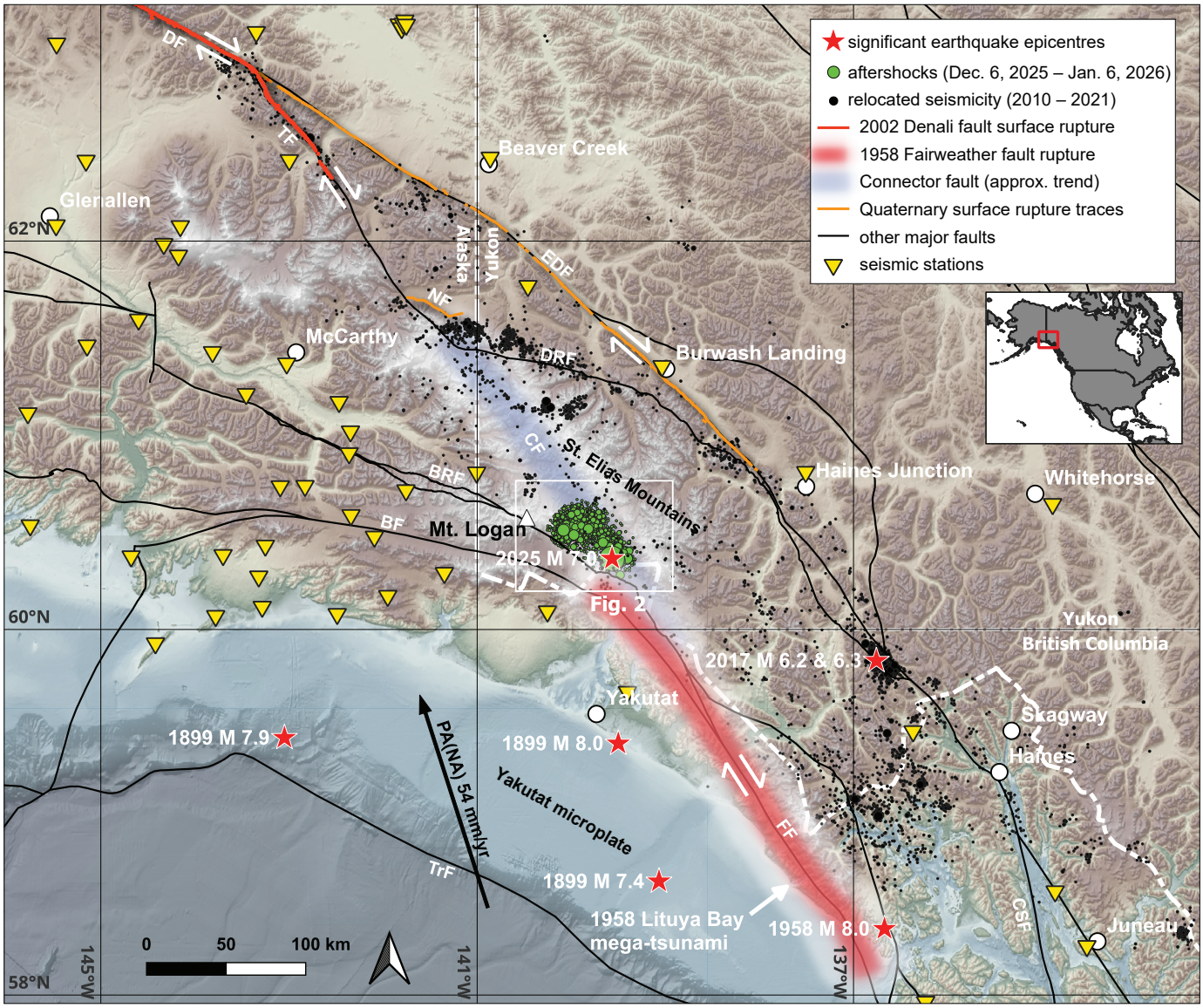

Figure 1. *Overview map of the regional tectonic setting of southwest Yukon and southeast Alaska including the December 6, 2025 mainshock and aftershock locations from the Natural Resources Canada (NRCan) earthquake catalogue. The approximate trace of the Connector fault (CF) is shown with the transparent blue polygon. Relocated background seismicity is from Biegel et al. (2024a). The 2002 M7.9 Denali fault (DF) rupture trace is from Haeussler (2009). The approximate 1958 M8 Fairweather fault (FF) rupture trace is from Doser (2010). The Eastern Denali fault (EDF) surface rupture traces are from Finley (2025). The Natazhat fault (NF) surface rupture trace is from Haeussler et al. (2024) based on Marechal et al. (2018). The locations of the 1899 earthquake sequence are from Doser (2006). Other major faults (black lines) are from the Yukon Geological Survey (2021): TF – Totschunda fault; DRF – Duke River fault; BRF – Border Ranges fault; BF – Bagley fault; TrF – Transition fault; CSF – Chatham Strait fault. Pacific Plate motion relative to North America (PA[NA]) is from the MORVEL model (DeMets et al., 2010).*

at the western margin of North America at a rate of >50 mm/yr. Further north, and to the west, the Pacific plate is subducting at the Alaska–Aleutian subduction zone. As a result, the tectonic regime of southwestern Yukon occupies a critical transition between transform motion, subduction, and continental collision, where the buoyant Yakutat crust exerts a strong control on upper-plate deformation (Plafker, 1987). Here, regional plate motion is partitioned between crustal shortening and a network of right-lateral strike-slip fault systems that accommodate lateral extrusion and strain transfer into the continental interior (Bruhn et al., 2012). It is within this remote, glaciated region of southwestern Yukon that the December 6, 2025 M_w7.0 earthquake occurred.

Earthquake-induced landslides in mountainous terrain

Earthquake-induced landslides are common in mountainous regions affected by shallow earthquakes, and represent a significant secondary hazard (Massey et al., 2018). When such events occur in populous regions, they have caused tens of thousands of deaths and significant economic losses beyond the direct effects of shaking (Keefer, 1984; Marano et al., 2010). Furthermore, in remote areas with limited transportation infrastructure, landslides can significantly impede emergency response to earthquakes if key roads are impacted (Bird and Bommer, 2004). Mapping landslide susceptibility can provide guidance on where the regions of highest hazard and risk are located (e.g., Behnia and Blais-Stevens, 2018). Additionally, earthquake-induced landslide prediction models can provide situational awareness to aid emergency response as well as generate estimates of landslide extent for hypothetical future earthquake scenarios (e.g., Nowicki Jessee et al., 2018). Such models are generally based upon empirical landslide inventories from past earthquakes. However, it is important to compile representative inventories for regions with specific climatic and geological conditions.

Many regions of the Yukon are susceptible to landslides (e.g., Brideau et al., 2026), particularly as slopes are becoming increasingly destabilized due to permafrost thaw (e.g., Clarke et al., 2024; Lipovsky and Huscroft, 2007). Moreover, many of Yukon's most active faults occur in mountainous terrain that could be susceptible to earthquake-induced landslides. For example, the Eastern Denali fault (EDF) occurs along the steep front range of the St. Elias Mountains (Fig. 1), posing a potential earthquake-induced landslide hazard to communities and infrastructure along the Alaska Highway corridor (Blais-Stevens et al., 2020; Finley, 2025). Potential earthquake-induced landslides related to prehistoric ruptures have been identified along the EDF (Everard, 1994; Whelan, 2022). More generally, landslides are known to threaten some of Yukon's communities (Brideau et al., 2007; Bodtker et al., 2023; Lipovsky, 2023) and though these are not necessarily linked to seismicity, it is important to understand how shaking might exacerbate the existing hazard. The December 6 event offers an opportunity to study seismically induced landslides in the Yukon.

Observations and interpretations

Seismic observations

The M_w7.0 mainshock occurred on December 6, 2025 at 20:41 UTC (13:41 Yukon Standard Time) at 60.37° N and 139.54° W, with a hypocentre location ~10 km east-northeast of Mt. Vancouver in the St. Elias Mountains (Fig. 1, Fig. 2). In this work, we consider 354 analyst-reviewed events drawn from the Natural Resources Canada (NRCan) National Earthquake Database (NEDB; Canadian Hazards Information Service, 1985), augmented by an additional 4193 automatic (i.e., not analyst reviewed) NRCan solutions within our study area between the occurrence of the mainshock on December 6, 2025 and the aftershocks of January 6, 2026 (Fig. 1).

To study the aftershock distribution, we use the double-difference (DD) relocation method (Waldhauser and Ellsworth, 2000), which improves relative precision for earthquake hypocentres. An advantage of the DD approach is that errors introduced by complex or unmodeled velocity structures along the propagation path from the earthquake source region to the recording station are reduced when proximal events are jointly relocated. The increased precision of relative hypocentre location can significantly improve event depths in otherwise sparsely instrumented settings (e.g., Biegel et al., 2024b) and can enable the identification and geometric characterization of discrete fault planes (e.g., Rubin et al., 1999; Biegel et al., 2024a). In the relocation, we use traditional arrival times for P and S-wave phases obtained from the NRCan solutions. These are supplemented with differential travel times based on waveform cross-correlations between event pairs. These data are jointly inverted using the SeisComP Real-Time Double-Difference (scrtdd) implementation of the DD algorithm (Scarabello et al., 2025; Helmholtz Centre Potsdam

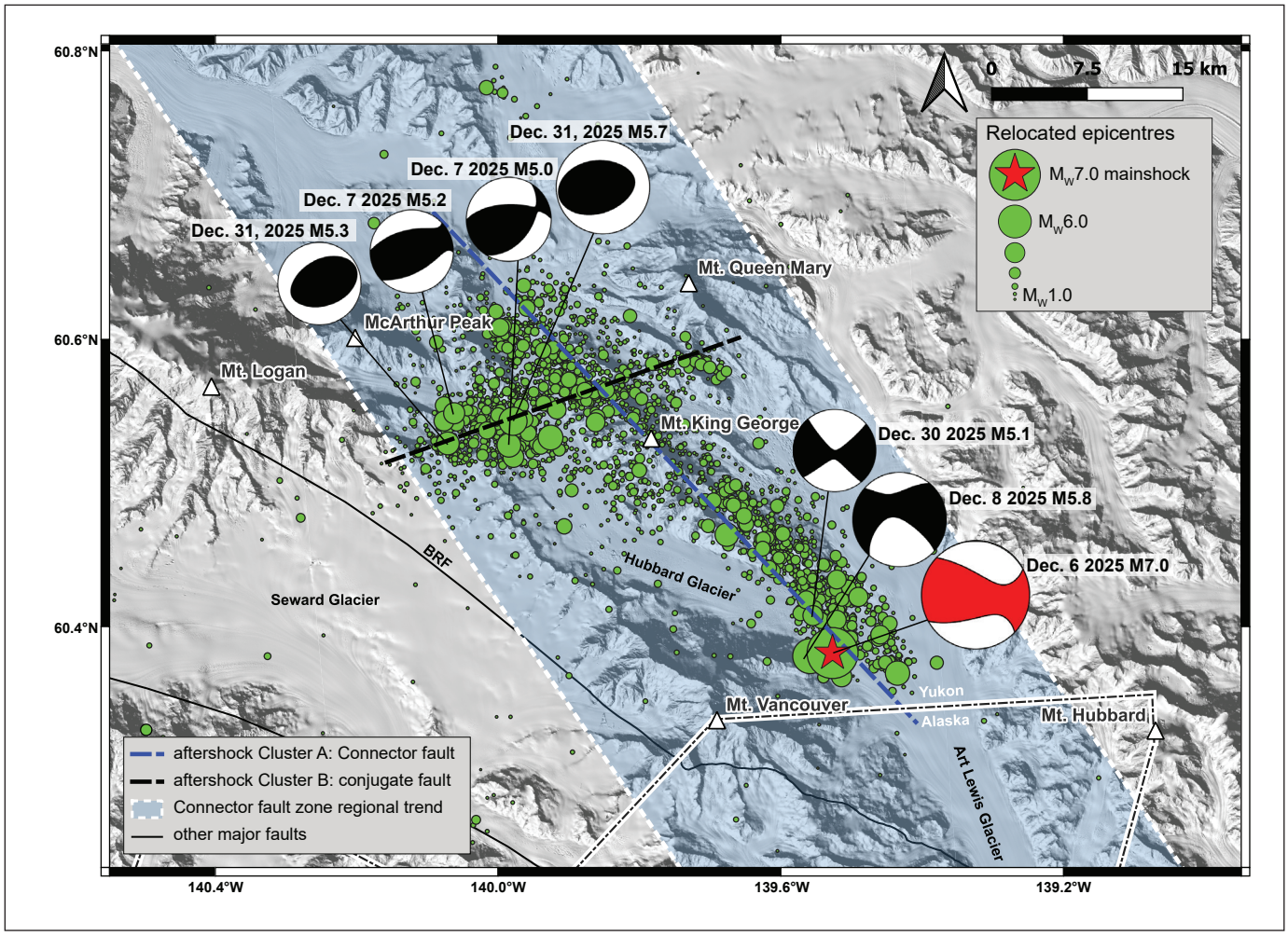

Figure 2. *Close-up view of the relocated aftershock sequence and inferred fault traces. The moment tensor (MT) solutions are shown for >M5 aftershocks where available (US Geological Survey, 2025a). See Figure 4 for 3D views of aftershocks. BRF – Border Ranges fault. Base map hillshade is from ArcticDEM version 4.1 (Porter et al., 2023).*

GFZ German Research Centre for Geosciences and gempa GmbH, 2008). For travel time predictions, we use the 1D seismic velocity model IASP91 (Kennett and Engdahl, 1991). Relocation algorithm parameters are mostly the same as in Schaeffer et al. (this volume). The only differences are an increased maximum number of neighbouring events per chain of 120, and reduced P and S-waveform cross correlation window lengths of ± 0.5s and ± 0.75s, respectively.

After relocation and application of quality control, 3280 aftershock locations are successfully updated (Fig. 2). The aftershocks mostly occurred to the northwest of the mainshock hypocentre and extended in this direction for ~50 km. Based on this observation, the mainshock rupture propagated toward the northwest and likely arrested in an area ~5 km east of McArthur Peak. To the northwest of Mt. King George, the distribution of epicentres is spread out laterally from this linear feature. An additional linear feature is apparent from the distribution of relocated aftershocks, particularly for events at the northwest end of the aftershock sequence. Overall, relocated event depths are predominantly shallower than 10 km, and the peak in the distribution of event depths occurs at ~4 km, supporting the shallow nature of the mainshock. The depth distribution is consistent with previous estimates of the crustal seismogenic layer thickness of <15 km in this area (Biegel et al., 2024b).

We carried out cluster analysis (e.g., Biegel et al. 2024a) of the relocated hypocentres. Clusters are first identified using the 'density-based spatial clustering of applications with noise' algorithm (DBSCAN; Ester et

al., 1996), in which the maximum distance to consider neighbours was set at 1.8 km, and the minimum number of neighbours to identify a cluster was set at 30. The DBSCAN algorithm identifies four potential clusters. Upon inspection, three of these clusters align along a single northwest–southeast structure and are reclassified as a single cluster. Because the remaining two clusters overlap, one fault planes is fit to each cluster using a least squares regression. Based on seismogenic layer thickness and distribution of relocated event depths, the maximum depth for the fault planes was chosen as 15 km. Subsequently, events are reclustered by proximity to one of these planes, and 10% of outlier events are excluded from the clustering based on the distance from the planes. Finally, we recalculate the least squares fits based on these re-sorted clusters which we name Cluster A and Cluster B (Fig. 3).

Using this clustering analysis, we identified two event clusters: Cluster A includes 1480 aftershocks, and Cluster B, 1155 aftershocks (Fig. 3). The remaining 270 aftershocks were unassigned. Cluster A has a dominant northwest–southeast-striking zone aligned with the inferred trace of the CF, and hosted the mainshock near its southern termination. The plane for Cluster A has a length of 60 km, a width of 15 km, and strike of 136°; the dip is 78° to the southwest. We interpret that this plane represents part of the CF. We note that a significant part of the fault plane solution for Cluster A is located beneath the Mt. King George massif. The fault for Cluster B is smaller in size and oriented at a conjugate strike of 250° with a dip of 86° to the north-northeast. The projected surface trace of the fault plane solution for both clusters is shown in Figure 2. We hypothesize that the mainshock may have included a complex rupture on multiple faults highlighted by the two clusters, but that the rupture initiated on the CF, and then triggered a rupture on a conjugate fault. The misfit from plane fitting for Cluster A is excellent, having an R2 value for the least squares planar fit of 0.95. However, misfit for Cluster B is lower (R2 = 0.39), and it is possible that multiple faults contribute to the poor least squares fit of Cluster B.

We further consider the spatial distribution of the largest aftershocks in the context of available MT solutions (Fig. 2). The MT solutions for the largest aftershocks along this feature exhibit dextral strike-slip mechanisms (Fig. 2). In contrast, the subsidiary conjugate lineament in the northwestern part of the aftershock cloud trends west-southwest to east-northeast and is associated with the largest aftershocks

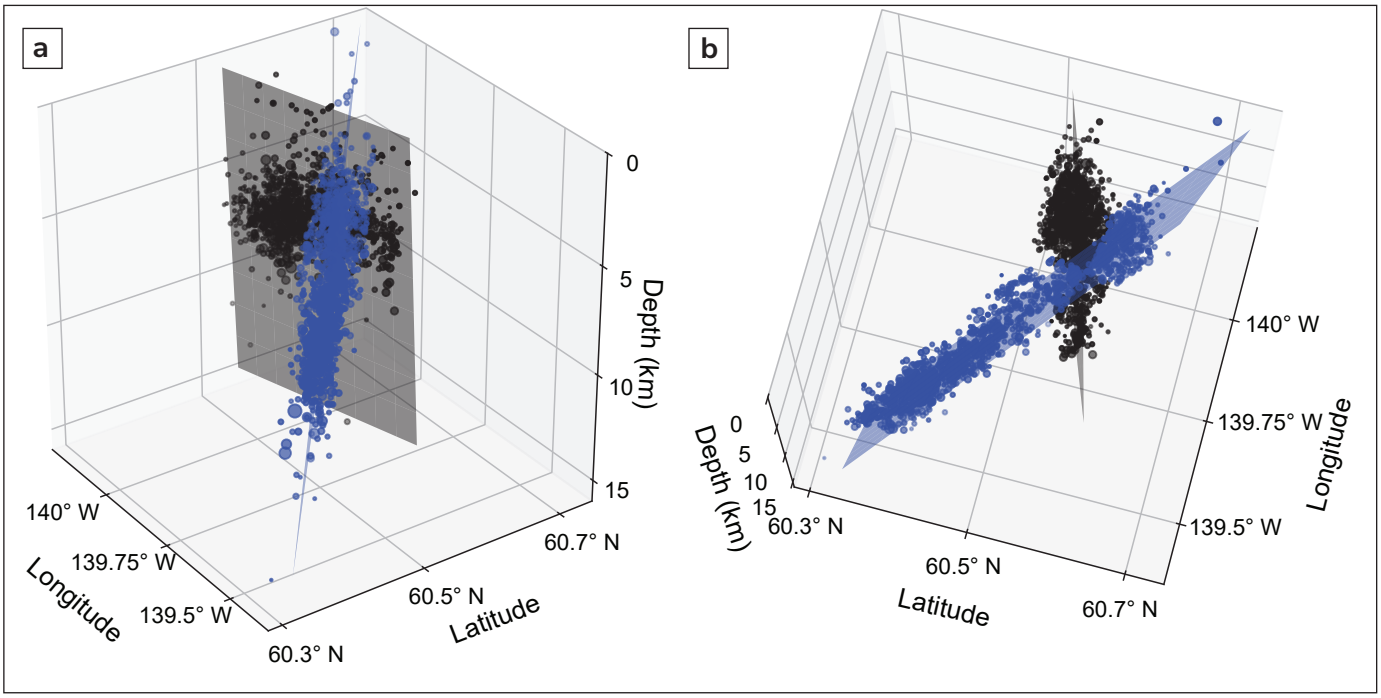

Figure 3. *Relocated aftershocks and inferred fault planes based on cluster analysis. Cluster A (blue) and Cluster B (black) are shown. Panel* ***(a)*** *view is oblique toward the northwest along strike of Cluster A fault plane. Panel* ***(b)*** *view is from overhead.*

exhibiting predominantly reverse mechanisms. Despite this variability in faulting style, available faulting mechanisms across the sequence share broadly similar P-axis orientations, consistent with a common regional stress field imposed by oblique convergence of the Yakutat microplate with North America (Gosselin et al., 2024). This pattern suggests rupture propagation and subsequent stress redistribution within a transpressional fault network, where strike-slip motion along the primary structure (CF) is locally accommodated or transferred onto conjugate, more contractional structures. The coexistence of strike-slip and reverse mechanisms, coupled with the segmented aftershock geometry, supports a model in which the December 6 earthquake activated multiple fault strands with differing orientations and kinematics within a shared regional stress regime. This hypothesis is further supported by the complexity of the MT solution of the mainshock, which exhibits oblique kinematics and suggests strain partitioning during a mechanically complex rupture process rather than slip on a single, planar fault. Furthermore, mainshock and some aftershock MT solutions show significant non-double-couple components, providing evidence that slip did not occur on a single, planar fault.

There does not appear to be a spatiotemporal pattern to the aftershock sequence between December 6 and December 31, 2025. However, a M_w5.7 aftershock on December 31 marked a resurgence in aftershock activity that is inconsistent with typical Omori-Utsu decay (Utsu et al., 1995). This event and the associated resurgence were located along the inferred conjugate fault planes with a reverse mechanism.

It is likely that the aftershock catalogue includes not only earthquakes but also landslides and cryospheric sources of seismic energy. To separate the various source types in the catalogue will require careful waveform examination that is currently ongoing. The superposition of multiple coincident seismic events complicates the analysis of seismic waveforms and can lead to a temporary increase in the magnitude of completeness of the earthquake catalogue. During our study period between December 6, 2025, and January 6, 2026, we note that there are two events of >M_w5 for which an MT solution is not reported. These events both occurred shortly after the mainshock on January 6, during a period of intense seismic activity that likely inhibited reliable MT estimation. The superposition of multiple seismic events may also preclude the conclusive assignment of source types in future analysis.

Surface effects and mass movement observations

Within minutes of the event on December 6, the US Geological Survey released an automated landslide probability map (Nowicki Jessee et al., 2018; Allstadt et al., 2022) that illustrated the elevated potential for landslides across a >2000 km^2 area with the highest probabilities on the slopes of Mt. Logan and Mt. Vancouver (US Geological Survey, 2025b). On December 9, Sentinel-1 radar change detection revealed numerous large slope failures (Eiden et al., 2025), though it was not immediately clear whether these were dominantly rock, ice or snow. With clearer weather, Landsat 8 and 9 images on December 10, 11 and 12 further confirmed the occurrence of numerous landslides. On December 12, the Yukon Geological Survey flew to the epicentral area to document the landslides and other surface effects before they could be obscured by further snowfall and glacial deformation. Our observations form the basis of a landslide inventory for this event.

Field observations on December 12, 2025 confirmed the occurrence of extensive landslides, snow and ice avalanches, and widespread damage to glaciers. Using satellite imagery (Landsat), our field observations, and nearly 2000 oblique aerial photographs taken from the helicopter, we map over 200 individual landslide initiation points and a subset of the largest runouts (Fig. 4). We distinguished landslides from snow and ice avalanches based on the texture and colour of the debris deposits, as well as the presence of a clear source-area scar in bedrock. Landslide activity was mainly concentrated on the Mt. King George massif (Fig. 4), where rock-ice avalanches and rockfall were the most common failure types. Bare rock was exposed on the majority of slopes of Mt. King George in contrast to surrounding peaks, which had largely retained their snow cover (Fig. 5).

The largest observed landslide was a rock and ice avalanche produced by a partial collapse of the southwest ridge of Mt. King George (Fig. 5a). The basal failure surface occurred along a southwest-dipping planar discontinuity oriented subparallel with the pre-existing slope angle (~35–40°) of the south flank of the ridge. The Mt. King George massif is underlain by Cambrian to Ordovician volcanic and sedimentary rocks which exhibit a northwest-striking foliation and dip between 30 and 60° to the northeast (Dodds and Campbell, 1992). The southwest flank of the massif is intruded by Jurassic to Cretaceous granite of the St. Elias plutonic suite. Notably the failure surface of

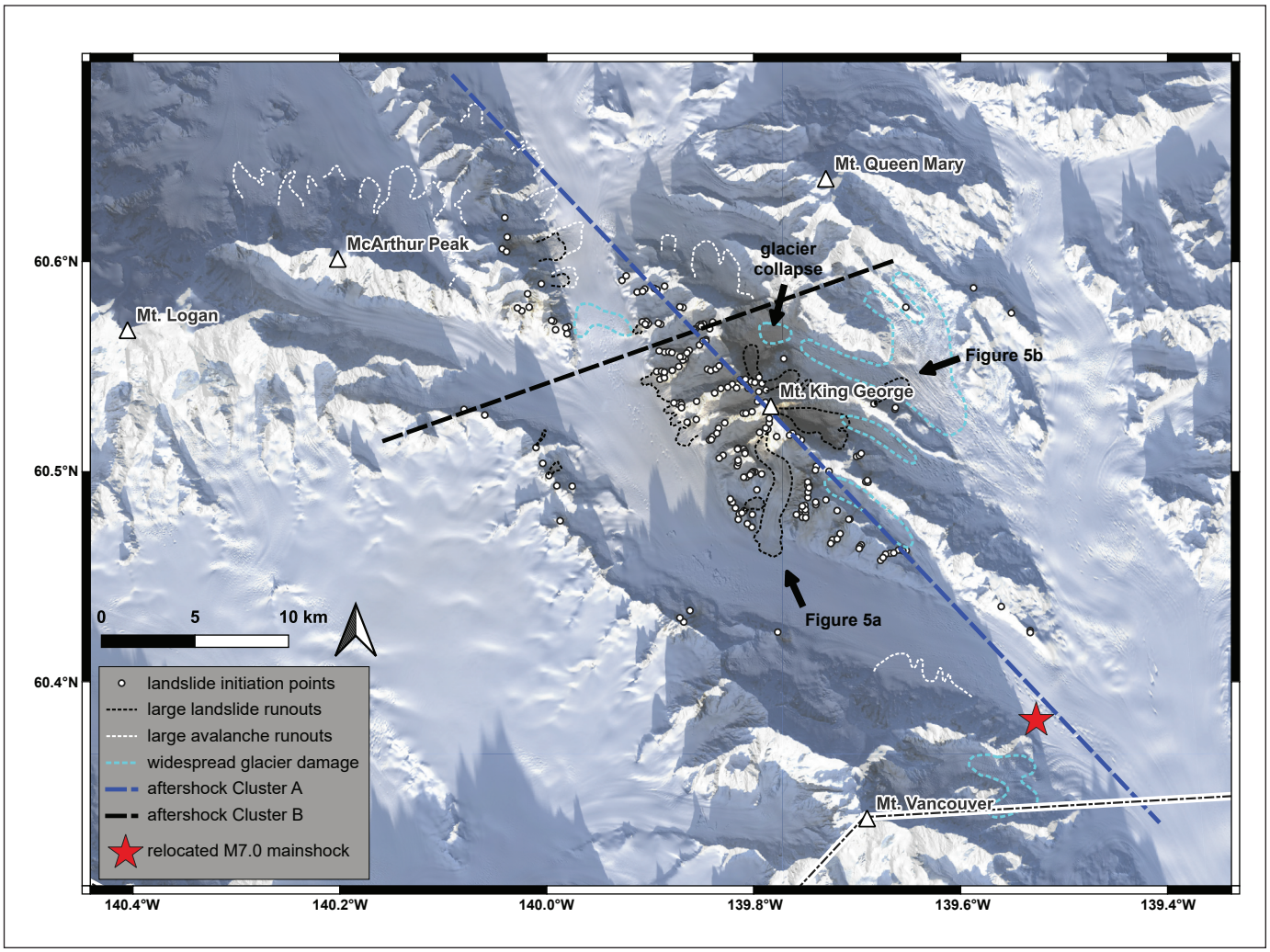

Figure 4. *Landslides and avalanches observed in the epicentral area during the December 12 reconnaissance flight. Landslides are concentrated around Mt. King George, whereas avalanches and areas of damaged glacial ice are more widespread. Base imagery is from a Landsat 8 pass on December 11, 2025.*

this slide is at a high angle to the local geological strike and dip, which was also apparent from the helicopter. The crown of the slide originated at approximately 3000 m above sea level and descended roughly 1300 m along a tributary glacier before coming to rest on the Hubbard Glacier, approximately 7.4 km from the source area (Fig. 5a). This corresponds to an overall travel angle of approximately 10°. Such high mobility is typical of rock avalanches on glaciers (Evans and Clague, 1988), where movement is enhanced by the low-friction surface of the glacier, entrainment of snow and ice, and by water inputs generated through frictional melting (Sosio et al., 2012). Several other rock and ice avalanches with similar mobility characteristics, but smaller overall dimensions, occurred in other tributary valleys on the southwest side of Mt. King George (Fig. 4).

On the northeast side of Mt. King George, several large rock falls and rock avalanches initiated on steep slopes (50–70°), falling at least 1700 m to the glacier below (Fig. 5b). Persistent rockfall and additional rock avalanches continued from existing slide scars for several days after the main earthquake, likely due to a combination of aftershocks and progressive failure of slopes that were damaged by the earthquake or destabilized by earlier failures. At least one entirely new rock avalanche occurred between December 11 and 12 as it only appeared on December 12 Landsat imagery and was apparent during our site visit (Fig. 5b). At the time of the overview flight, large dust clouds lingered in the air, obscuring our view of debris deposits on the glacier below (Fig. 5b). The large, active slide scar on the east face of the Mt. King George summit appeared to have water flowing down its centre,

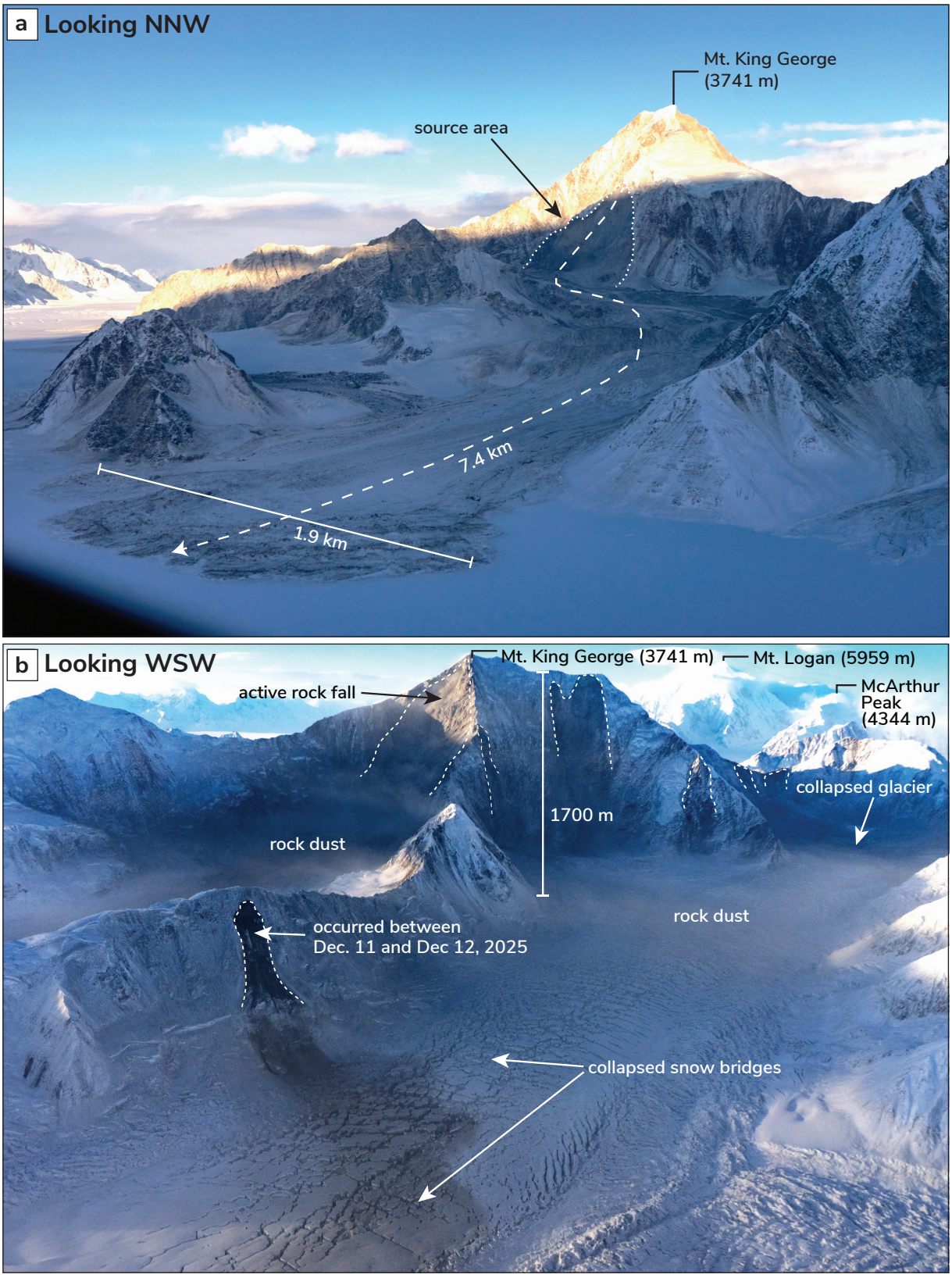

Figure 5. *Photos from December 12 reconnaissance flight over epicentral area:* ***(a)*** *largest landslide on west side of Mt. King George looking north-northwest (NNW); and* ***(b)*** *east side of Mt. King George looking west-southwest (WSW). White dashed lines indicate landslide source areas. See Figure 4 for photo locations.*

suggesting either discontinuous permafrost within the massif, or significant heating associated with slope failure. Beyond the Mt. King George massif, landslides were relatively limited. Two large landslides occurred on the east side of McArthur Peak, and several small point-source slides occurred on the arête between Mt. Vancouver and Mt. Logan (Fig. 4).

Snow avalanches were triggered in a much more extensive region than landslides (Fig. 4). Some of the largest snow avalanches occurred on the north and east aspects of Mt. King George and McArthur Peak (a sub-peak of Mt. Logan) and produced plumes that in some cases extended 2–3 km across the glacier at the base of the slopes from which they fell, covering hundreds of hectares each (Fig. 4). Based on their runout length and plume area, some of these avalanches are likely size 5, the largest and most destructive on the Canadian snow avalanche classification scale (Stethem et al., 2003). The apparent preference for aspect and the concentration of large avalanches at the northwest tip of the rupture could be related to directivity effects of strike-slip fault motion (e.g., Velasco et al., 2004), or simply local snowpack conditions at the time of the earthquake.

Damage to glaciers was also extensive; seracs (blocks and columns of ice between crevasses) were broken up and toppled by shaking, and in several locations, snow bridges over crevasses had collapsed (Fig. 5b). Particularly large areas of ice damage occurred on the east sides of Mt. King George and Mt. Vancouver (Fig. 4). There were also widespread failures of cornices and ice accumulations on ridgelines. Additionally, fresh cracking was observed at numerous ice-rock contacts at the margins of glaciers, possibly reflecting settling or dislodging of ice during shaking.

Despite the shallow rupture indicated by mainshock and aftershock relocations, we observed no clear evidence of fault surface rupture. However, it is possible that a surface rupture was hidden by thick glacial ice; adjacent glaciers in the St. Elias Mountains have been estimated to have thicknesses of >900 m based on airborne ice penetrating radar (Christine Dow, pers. comm.). Moreover, because the rupture appears to be directly beneath Mt. King George, a clear surface rupture could be obscured by the rugged topography and subsequent widespread slope failures. The apparent structural immaturity of the fault zone may also play a role in reducing its surface expression (e.g., Sethanant et al., 2023). Notably, a partial collapse of a low-angle glacier surface occurred between Mt. King George and Mt. Queen Mary (Fig. 4), an area adjacent to many of the most intense aftershocks at the intersection of the two linear clusters. It is conceivable that this collapse is related to a fault surface rupture beneath the glacier. However, this area of the glacier is covered by debris from a rock avalanche off the northeast face of Mt. King George, which could have also contributed to its collapse.

Discussion

Implications for the Connector fault, regional tectonics, and seismic hazard

The occurrence of the December 6 earthquake offers insight into the geometry and kinematics of the long-hypothesized CF that links the Fairweather and Totschunda fault systems and enables transfer of strike-slip motion. The concept attempts to reconcile plate-boundary kinematics across southeast Alaska and southwestern Yukon (Grantz, 1966; Richter and Matson, 1971; Lahr and Plafker, 1980). These early models provide a tectonically coherent explanation for how relative motion between the Pacific, North America, and Yakutat plates could be partitioned. This early work evolved into later plate-boundary reconstructions that emphasized distributed deformation (e.g., Marechal et al., 2015). However, subsequent regional syntheses continued to invoke a Fairweather–Totschunda linkage to explain long-term strain transfer and seismic moment balance in the region (e.g., Fletcher and Freymueller, 2003). Subsequent earthquake relocations by Doser (2014) delineated a possible trace of the CF. With improvements to the seismic network (Meighan et al., 2013; Busby and Aderhold, 2020), Biegel et al. (2024a) were able to relocate a larger catalogue of earthquakes (Fig. 1) and proposed a fault trace slightly west of that proposed by Doser (2014).

Geodetic observations provide independent support for the existence of the CF (e.g., Elliot et al., 2010; Elliott and Freymueller, 2020). In these tectonic block models, the proposed CF coincides with a zone of elevated shear strain and serves as a kinematic boundary between blocks rotating at different rates. Although the fault cannot be resolved as a single sharp velocity gradient from these data, its location is broadly consistent with subtle geomorphic lineaments that suggest long-term structural control. Similar geomorphic expressions characterize other intracontinental strike-slip transfer zones in Alaska and western North America, where cumulative slip is modest or partitioned across multiple strands, limiting the development of a clear surface

trace (e.g., Bemis et al., 2015; Koehler et al., 2012). Identification of a geomorphic expression along the CF is further complicated by its location in a remote, heavily glaciated region, where repeated glacial erosion and sediment redistribution can obscure or entirely remove surface fault scarps and offset landforms (Haeussler et al., 2008; Haeussler et al., 2017). The 2023 US National Seismic Hazard Model includes a discrete fault source representing the CF with a 13 mm/yr slip rate (Haeussler et al., 2024). Their fault trace is largely based on that of Doser (2014) and follows the trends of major valley glaciers as well as seismicity; however, they acknowledge there is uncertainty on its absolute location.

The December 6 M_w7.0 earthquake provides the clearest observational evidence to date for the existence, geometry, and kinematics of the long-postulated CF. Relocated aftershocks define a dominant northwest–southeast-trending structure consistent with the inferred regional trend of the CF (Fig. 2), with the mainshock initiating near its southern end and rupture propagating northward. Available MT solutions (US Geological Survey, 2025a) along the CF indicate predominantly strike-slip motion near the mainshock, transitioning to thrust-dominated mechanisms further northward, along conjugate structures. The activation of a subsidiary, east–west-oriented aftershock lineament suggests strain partitioning within this intracontinental transfer zone and highlights the likelihood of stress redistribution to adjacent faults. This concept is being evaluated through ongoing Coulomb stress modelling.

Importantly, this earthquake occurred on a structure lacking a previously mapped surface trace and within a local area of comparatively sparse historical seismicity, underscoring both the cryptic nature of the CF and its capacity to host large earthquakes. While Biegel et al. (2024a) documented a northern segment of the CF south of the Totschunda fault terminus based on relocated background seismicity (Fig. 1), the December 6 event demonstrates that this structure is through-going. Most previous studies (e.g., Doser, 2014; Haeussler et al., 2024) have inferred that the trace of the CF in this area occurs beneath, and is obscured by, the major valley glaciers (Hubbard and others). However, our earthquake relocations suggest that this segment of the fault is situated beneath the Mt. King George massif, and the landslide distribution further corroborates this location. The lack of a pre-existing surface expression could reflect the fact that erosion rates in this mountainous region are high, and preservation potential is limited. Moreover, it has been suggested that the CF is an incipient fault that is taking up strain that was previously accommodated by the Eastern Denali fault (Richter and Matson, 1971; Choi et al., 2021). The lack of clear topographic expression could therefore also reflect the structural immaturity of this developing fault zone.

Although the region in the immediate vicinity of the earthquake is uninhabited, this event presents several seismic hazard considerations. The southern tip of the rupture is 20–30 km from the approximate northern termination of the 1958 Fairweather fault ~M8.0 rupture (Doser, 2010). There is likely a large degree of spatial uncertainty on the northern part of the 1958 rupture. Doser (2010) places it on the main strand of the Fairweather fault (as depicted in Fig. 1), though it could conceivably have branched onto an eastern splay of the Fairweather fault mapped beneath the Art Lewis glacier (US Geological Survey, 2026), which is more directly aligned with the 2025 rupture (Fig. 2). Nevertheless, there appears to be a gap between the 1958 and 2025 ruptures that could have a lingering slip deficit, and Coulomb stress changes following the recent earthquake could promote future failure. Earthquake scaling relations indicate a 30 km fault length could cause an ~M6.8 earthquake, assuming a crustal seismogenic thickness of 15 km (Wells and Coppersmith, 1994). This section of fault passes near the heads of several glaciated fjords (Disenchantment Bay and Nunatak Fjord) where there is the potential for landslide generated tsunamis not unlike the 1958 Lituya Bay megatsunami (Fig. 1; Miller, 1960), or the recent Tracy Arm landslide southeast of Juneau (Read et al., 2025). To the north, there is an ~225 km section of fault between the 2025 rupture and the southern termination of the 2002 Denali earthquake on the Totschunda fault (Fig. 1). Geomorphic mapping by Marechal et al. (2018) provided evidence of rupture within the Quaternary on this section. If the entire section were to rupture at once, it could cause an ~M7.7 earthquake (Wells and Coppersmith, 1994); however, given the apparent structural immaturity, it is unclear whether it would do so in a single event, or in smaller sections.

Due to the remote location of the earthquake, no damage was reported (Natural Resources Canada, 2025). Ground shaking from the mainshock and several aftershocks was reported in the communities of Haines Junction, Burwash Landing and Whitehorse. However, the earthquake serves as a reminder of the seismic hazard in southwest Yukon, and the need to assess local variability of earthquake shaking intensity and duration due to site-specific geologic conditions (e.g., Gosselin et al., 2025; Byer et al., this volume).

This earthquake also offers an opportunity for ongoing research that compares ground-motion predictions to felt reports (specifically in the Yukon), which can improve estimates of shaking during more-damaging events that may occur in the future.

Relationships between mass movement and fault rupture

Based on our aftershock relocations, the Mt. King George massif directly overlies the fault rupture, and the landslide distribution is therefore reflective of the region where shaking was the strongest. Empirical relationships between earthquake magnitude and landslide distribution (Keefer, 1984; Rodriguez et al., 1999; Keefer, 2002) suggest that for a M7 earthquake, landslide activity is expected over an area between 1000 and 10 000 km^2. Our field observations indicate that the landslide distribution for this event was on the low end: the core area of landslides occurred over approximately 200 km^2 on the Mt. King George massif, and the most distal landslides occurred within an area of 500 km^2. The empirical data from past earthquakes further indicates that for M7 earthquakes, the expected maximum distance between the epicentre and rock falls and rock avalanches is between 100 and 200 km. Our field observations again place this event well below that, with a maximum distance of 35 km between the epicentre east of Mt. Vancouver, and the rock falls observed on the east side of McArthur peak. Measuring from the fault rupture plane defined by the aftershocks, maximum distances of 75 to 150 km are expected; however, in the case of this earthquake, maximum distances were around 11 km between the rupture plane and small landslides observed on the arête between Mt. Vancouver and Mt. Logan (Fig. 4). When compared to maps of shaking intensity, rock falls and rock avalanches typically require shaking of at least 4 on the Modified Mercalli Index (MMI), and the majority occur in zones of MMI 5 or greater. On the initial isoseismal maps generated by the US Geological Survey (2025b), MMI values of 5 occurred over an area >15 000 km^2, whereas the majority of landslides in this event occurred within the much smaller zone of MMI 7 or greater. It is worth noting however, that the sparse instrumentation in the epicentral region provides poor constraint on shaking intensity. The anomalously small area with seismically induced landslides may be due to the shallow depth of the rupture. Keefer (1984) observed that earthquakes with greater focal depths allow for sufficient shaking to trigger landslides over broader areas. We also speculate that local geological and climatic conditions (i.e., extreme cold and permafrost) may play a role in limiting the extent of landslides in this particular case study.

The US Geological Survey ground failure product estimates earthquake-induced landslide probability in near real-time based on estimated peak ground velocity (PGV) for the earthquake. It also considers global datasets of slope, lithology, land cover, climate, and soil wetness (Nowicki Jessee et al., 2018; Allstadt et al., 2022). Such a model could be applied proactively to earthquake hazard and risk scenarios for Yukon faults and the surrounding affected communities. Additionally, it could serve as a critical part of emergency response in future earthquakes. Nowicki Jessee et al. (2018) call for the collection of new comprehensive landslide inventories to improve the accuracy of these models, as well as inform region-specific models that take into consideration local variations in climate and geology. It is a goal of the Yukon Geological Survey to finalize the landslide inventory for this event to improve our understanding of potential hazard cascades faced by Yukon communities.

Conclusion

The December 6, 2025 M_w7.0 earthquake in southwestern Yukon was the largest continental earthquake in Canada in several decades and provides a rare opportunity to examine active tectonic processes in a remote, glaciated region. This earthquake sequence provides the most conclusive evidence to date for the existence and activity of the long-hypothesized Connector fault (CF), demonstrating that it is a through-going structure capable of hosting large-magnitude earthquakes despite the absence of a clear surface trace. Seismological observations indicate that this event involved a mechanically complex rupture, reflected by a large non-double-couple moment tensor solution. Analysis of relocated aftershocks (including relocation, cluster analysis, and fault-plane regression fitting), combined with available moment tensor solutions for the largest aftershocks suggests rupture occurred on at least two distinct fault segments. The mainshock initiated at the southern end of a southeast-striking segment of the CF and was dominated by dextral strike-slip motion, while the main event and subsequent aftershocks also activated an east-striking conjugate fault with reverse motion. The rupture complexity may reflect the structural immaturity of this incipient fault zone.

The shallow depth of rupture and its occurrence within a heavily glaciated, high-relief landscape led to widespread surface effects, including landslides and snow avalanches; preliminary observations indicate that these effects were concentrated near the Mt. King George massif. Notably, the areal extent of landslides

was considerably smaller than predicted based on empirical relations from past earthquakes, possibly due to the midwinter timing and widespread permafrost. Despite the shallow hypocentral depth, no surface rupture was observed, though it may be obscured by glacial ice or rugged topography. The damage to glacial ice, continuing rock fall, and lingering seismic hazard on adjacent fault segments will potentially pose an ongoing hazard for mountaineers and skiers who frequent the area. More broadly, the December 6, 2025 earthquake underscores the need for increased earthquake hazard awareness and preparedness in northern Canada, where large events may occur on unmapped or cryptic structures. Future research should focus on the integrated assessments of seismic hazard that explicitly consider interactions among earthquakes, landslides, geological site conditions, and climate-driven processes such as permafrost thaw, which may further exacerbate slope instability and compound risk in a rapidly changing Arctic and sub-Arctic environment.

Acknowledgments

This research occurred on the Traditional Territory of the Kluane First Nation. We thank Kate Allstadt, Elizabeth Eiden, Erin Jensen and other staff from the US Geological Survey for providing rapid satellite-based landslide mapping in support of our reconnaissance flight to the area. Horizon Helicopters provided a safe flight in extreme, cold conditions. We are very grateful to Leyla Weston and Amy Stuart for facilitating this last-minute addition to the Yukon Exploration and Geology volume.

References

Allstadt, K.E., Thompson, E.M., Jibson, R.W., Wald, D.J., Hearne, M., Hunter, E.J., Fee, J., Schovanec, H., Slosky, D. and Haynie, K.L., 2022. The US Geological Survey ground failure product: Near-real-time estimates of earthquake-triggered landslides and liquefaction. Earthquake Spectra, vol. 38, no. 1, p. 5–36, https://doi.org/10.1177/87552930211032685.

Behnia, P. and Blais-Stevens, A., 2018. Landslide susceptibility modelling using the quantitative random forest method along the northern portion of the Yukon Alaska Highway Corridor, Canada. Natural Hazards, vol. 90, p. 1407–1426, https://doi.org/10.1007/s11069-017-3104-z.

Bemis, S.P., Weldon, R.J. and Carver, G.A., 2015. Slip partitioning along a continuously curved fault: Quaternary geologic controls on Denali fault system slip partitioning, growth of the Alaska Range, and the tectonics of south-central Alaska. Lithosphere, vol. 7, no. 3, p. 235–246, https://doi.org/10.1130/L352.1.

Biegel, K.M., Dettmer, J., Igonin, N. and Eaton, D.W., 2024a. Double-pair double-difference relocation improves depth precision and highlights detailed 3D fault geometry for induced seismicity in Alberta, Canada. Seismological Research Letters, vol. 96, no. 3, p. 100–112, https://doi.org/10.1785/0220240194.

Biegel, K.M., Gosselin, J.M., Dettmer, J., Colpron, M., Enkelmann, E. and Caine, J.S., 2024b. Earthquake relocations delineate a discrete fault network and deformation corridor throughout southeast Alaska and southwest Yukon. Tectonics, vol. 43, no. 5, https://doi.org/10.1029/2023TC008140.

Bird, J.F. and Bommer, J.J., 2004. Earthquake losses due to ground failure. Engineering Geology, vol. 75, no. 2, p. 147–179, https://doi.org/10.1016/j.enggeo.2004.05.006.

Blais-Stevens, A., Clague, J.J., Brahney, J., Lipovsky, P., Haeussler, P.J. and Menounos, B., 2020. Evidence for large Holocene earthquakes along the Denali fault in southwest Yukon, Canada. Environmental and Engineering Geoscience, vo. 26, no. 2, p. 149–166, https://doi.org/10.2113/EEG-2263.

Bodtker, J., Cronmiller, D.C., Bond, J.D. and Shugar, D., 2023. The Sunnydale landslide, current understanding and research, Dawson (NTS 116B/3). *In:* Yukon Exploration and Geology 2022, K.E. MacFarlane (ed.), Yukon Geological Survey, p. 19–33.

Brideau, M.-A., Stead, D., Stevens, V., Roots, C., Lipovsky, P. and VonGaza, P., 2007. The Dawson City landslide (Dawson map area, NTS 116B/3), central Yukon. *In:* Yukon Exploration and Geology 2006, D.S. Emond, L.L. Lewis, and L.H. Weston (eds.), Yukon Geological Survey, p. 123–137.

Brideau, M.-A., Brayshaw, D., Hancock, C.-A., Lipovsky, P., Cronmiller, D., Lewkowicz, A., Blais-Stevens, A., Guthrie, R., Geertsema, M., Goetz, J., McGregor, C., Tannant, D., Friele, P., Clarke, J., Steelquist, A., Wong-Teichroeb, H., Ring, C. and Wells, G., 2026. Preliminary Canadian landslide database (13.0). Zenodo, https://doi.org/10.5281/zenodo.18216956.

Bruhn, R.L., Sauber, J., Cotton, M.M., Pavlis, T.L., Burgess, E., Ruppert, N. and Forster, R.R., 2012. Plate margin deformation and active tectonics along the northern edge of the Yakutat terrane in the Saint Elias orogen, Alaska, and Yukon, Canada. Geosphere, vol. 8, no. 6, p. 1384–1407, https://doi.org/10.1130/GES00807.1.

Busby, R.W. and Aderhold, K., 2020. The Alaska transportable array: As built. Seismological Research Letters, vol. 91, no. 6, p. 3017–3027, https://doi.org/10.1785/0220200154.

Byer, J.F., Gosselin, J.M., Dettmer, J. and Gilbert, H., 2026 (*this volume*). Preliminary investigation of seismic site conditions in Whitehorse (Kwänlin), Yukon, from passive seismic methods. *In:* Yukon Exploration and Geology 2025, A. Stuart, L.H. Weston and S.K. Schultz (eds.), Yukon Geological Survey, Government of Yukon, p. 119–130.

Canadian Hazards Information Service, 1985. Canadian National Earthquake Database. Natural Resources Canada, https://doi.org/10.17616/R3TD24, [accessed 08/01/2026].

Cassidy, J.F., Rogers, G.C., Lamontagne, M., Halchuk, S. and Adams, J., 2010. Canada's earthquakes: 'The good, the bad, and the ugly.' Geoscience Canada, vol. 37, no. 1, p.1–16.

Choi, M., Eaton, D.W. and Enkelmann, E., 2021. Is the Eastern Denali fault still active? Geology, vol. 49, no. 6, p. 662–666, https://doi.org/10.1130/G48461.1.

Christeson, G.L., Gulick, S.P., van Avendonk, H.J., Worthington, L.L., Reece, R.S. and Pavlis, T.L., 2010. The Yakutat terrane: Dramatic change in crustal thickness across the Transition fault, Alaska. Geology, vol. 38, no. 10, p. 895–898, https://doi.org/10.1130/G31170.1.

Clarke, H.C., Cronmiller, D.C., Ward, B.C. and Groeneveld, K.A, 2024. Permafrost-related landslides following a 2017 wildfire, Dempster Highway, Yukon (parts of NTS 116G/9 and 116H/12). *In:* Yukon Exploration and Geology Technical Papers 2023, L.H. Weston and Purple Rock Inc. (eds.), Yukon Geological Survey, p. 17–36.

DeMets, C., Gordon, R.G. and Argus, D.F., 2010. Geologically current plate motions. Geophysical Journal International, vol. 181, no. 1, p. 1–80, https://doi.org/10.1111/j.1365-246X.2009.04491.x.

Dodds, C.J. and Campbell, R.B., 1992. Geology, Mount St. Elias Map Area (115B &C[E1/2]), Yukon Territory. Geological Survey of Canada, Open File 2189, https://doi.org/10.4095/133475.

Doser, D.I., 2006. Relocations of earthquakes (1899–1917) in south-central Alaska. Pure and Applied Geophysics, vol. 163, no. 8, p. 1461–1476, https://doi.org/10.1007/s00024-006-0085-3.

Doser, D.I., 2010. A reevaluation of the 1958 Fairweather, Alaska, earthquake sequence. Bulletin of the Seismological Society of America, vol. 100, no. 4, p. 1792–1799, https://doi.org/10.1785/0120090343.

Doser, D.I., 2014. Seismicity of southwestern Yukon, Canada, and its relation to slip transfer between the Fairweather and Denali fault systems. Tectonophysics, vol. 611, p. 121–129, https://doi.org/10.1016/j.tecto.2013.11.018.

Eberhart-Phillips, D., Christensen, D.H., Brocher, T.M., Hansen, R., Ruppert, N.A., Haeussler, P.J. and Abers, G.A., 2006. Imaging the transition from Aleutian subduction to Yakutat collision in central Alaska, with local earthquakes and active source data. Journal of Geophysical Research: Solid Earth, vol. 111, no. B11, https://doi.org/10.1029/2005JB004240.

Eiden, E., 2025. Co-polarized synthetic aperture radar (SAR) change map between 11/28/2025 and 12/09/2025, Hubbard Glacier earthquake: US Geological Survey provisional data release, https://doi.org/10.5066/P14H7MVU.

Elliott, J.L., Larsen, C.F., Freymueller, J.T. and Motyka, R.J., 2010. Tectonic block motion and glacial isostatic adjustment in southeast Alaska and adjacent Canada constrained by GPS measurements. Journal of Geophysical Research: Solid Earth, vol. 115, no. B9, https://doi.org/10.1029/2009JB007139.

Elliott, J. and Freymueller, J.T., 2020. A block model of present-day kinematics of Alaska and western Canada. Journal of Geophysical Research: Solid Earth, vol. 125, no. 7, https://doi.org/10.1029/2019JB018378.

Enkelmann, E., Garver, J.I. and Pavlis, T.L., 2008. Rapid exhumation of ice-covered rocks of the Chugach-St. Elias orogen, southeast Alaska. Geology, vol. 36, no. 12, p. 915–918.

Ester, M., Kriegel, H.-P., Sander, J. and Xu, X., 1996. A density-based algorithm for discovering clusters in large spatial databases with noise. *In:* Proceedings of the 2nd International Conference on Knowledge Discovery and Data Mining (KDD-96), E. Simoudis, J. Han and U. Fayyad (eds.), p. 226–231.

Evans, S.G. and Clague, J.J., 1988. Catastrophic rock avalanches in glacial environments. *In:* Proceedings of the Fifth International Symposium on Landslides, Lausanne, Switzerland, vol. 2, p. 1153–1158.

Everard, K.A., 1994. Regional characterization of large landslides in southwest Yukon, with emphasis on the role of neotectonics. PhD thesis, University of British Columbia, Vancouver, British Columbia, Canada, 165 p.

Finley, T., 2025. Neotectonics of major faults in the Canadian Cordillera. PhD thesis, University of Victoria, British Columbia, Canada, 151 p.

Finzel, E.S., Trop, J.M., Ridgway, K.D. and Enkelmann, E., 2011. Upper plate proxies for flat-slab subduction processes in southern Alaska. Earth and Planetary Science Letters, vol. 303, no. 3–4, p. 348–360, doi:10.1016/j.epsl.2011.01.014.

Fletcher, H.J. and Freymueller, J.T., 2003. New constraints on the motion of the Fairweather fault, Alaska, from GPS observations. Geophysical Research Letters, vol. 30, no. 3, https://doi.org/10.1029/2002GL016476.

Gosselin, J.M., Biegel, K.M., Dettmer, J., Gilbert, H., Colpron, M. and Enkelmann, E., 2024. Crustal stress near the Yakutat microplate collision from probabilistic earthquake focal mechanisms. Canadian Journal of Earth Sciences, vol. 62, no. 4, p. 807–820, https://doi.org/10.1139/cjes-2024-0095.

Gosselin, J.M., Dettmer, J., Lipovsky, P. and Cronmiller, D., 2025. Seismic site amplification assessment in the Dakwäkäda (Haines Junction) area of Yukon, Canada, from probabilistic inference of passive seismic measurements. Canadian Geotechnical Journal, https://doi.org/10.1139/cgj-2025-0357.

Grantz, A., 1966. Strike-slip faults in Alaska, US Geological Survey Open File Report 66-53, 82 p.

Haeussler, P.J., Freymueller, J.T., Wesson, R.L. and Ekström, G., 2008. An overview of the neotectonics of interior Alaska: Far-field deformation from the Yakutat microplate collision. Active Tectonics and Seismic Potential of Alaska: American Geophysical Union Geophysical Monograph, p. 83–108.

Haeussler, P.J., 2009. Surface rupture map of the 2002 M7.9 Denali Fault earthquake, Alaska; digital data: US Geological Survey Data Series 422, http://pubs.usgs.gov/ds/422/.

Haeussler, P.J., Matmon, A., Schwartz, D.P. and Seitz, G.G., 2017. Neotectonics of interior Alaska and the late Quaternary slip rate along the Denali fault system. Geosphere, vol. 13, no. 5, p. 1445–1463, https://doi.org/10.1130/GES01447.1.

Haeussler, P.J., Bender, A.M., Powers, P.M., Koehler, R.D. and Brothers, D.S., 2024. Updating the crustal fault model for the 2023 national seismic hazard model for Alaska. *In:* Tectonics and Seismicity of Alaska and Western Canada: Earthscope and Beyond, N.A. Ruppert, M.A. Jadamec, and J.T. Freymueller (eds.), John Wiley & Sons Inc.

Helmholtz Centre Potsdam GFZ German Research Centre for Geosciences and gempa GmbH, 2008. The SeisComP seismological software package, GFZ Data Services, https://doi.org/10.5880/GFZ.2.4.2020.003.

Keefer, D., 1984. Landslides caused by earthquakes. Geological Society of America Bulletin, vol. 95, p. 406–421.

Keefer, D.K., 2002. Investigating landslides caused by earthquakes—A historical review. Surveys in Geophysics, vol. 23, no. 6, p. 473–510, https://doi.org/10.1023/A:1021274710840.

Kennett B.L.N. and Engdahl E.R., 1991. Traveltimes for global earthquake location and phase identification. Geophysical Journal International, vol. 105, no. 2, p. 429–465, https://doi.org/10.1111/j.1365-246X.1991.tb06724.x.

Koehler, R.D., Farrell, R.-E., Burns, P.A.C. and Combellick, R.A., 2012. Quaternary faults and folds in Alaska: A digital database. Miscellaneous Publication 141, Alaska Division of Geological & Geophysical Surveys, 33 p.

Lahr, J.C. and Plafker, G., 1980. Holocene Pacific–North American plate interaction in southern Alaska: Implications for the Yakataga seismic gap. Geology, vol. 8, no. 10, p. 483–486, https://doi.org/10.1130/0091-7613(1980)8%3C483:HPAPII%3E2.0.CO;2.

Lipovsky, P. and Huscroft, C., 2007. A reconnaissance inventory of permafrost-related landslides in the Pelly River watershed, central Yukon. *In:* Yukon Exploration and Geology 2006, D.S. Emond, L.L. Lewis and L.H. Weston (eds.), Yukon Geological Survey, p. 181–195.

Lipovsky, P.S., 2023. Surficial geology and geohazards of the greater Whitehorse area. Yukon Geological Survey, Open File 2023-1, 67 p. plus appendices.

Marano, K.D., Wald, D.J. and Allen, T.I., 2010. Global earthquake casualties due to secondary effects: A quantitative analysis for improving rapid loss analyses. Natural Hazards, vol. 52, no. 2, p. 319–328, https://doi.org/10.1007/s11069-009-9372-5.

Marechal, A., Mazzotti, S., Elliott, J.L., Freymueller, J.T. and Schmidt, M., 2015. Indentor-corner tectonics in the Yakutat-St. Elias collision constrained by GPS. Journal of Geophysical Research: Solid Earth, vol. 120, no. 5, p. 3897–3908, https://doi.org/10.1002/2014JB011842.

Marechal, A., Ritz, J.-F., Ferry, M., Mazzotti, S., Blard, P.-H., Braucher, R. and Saint-Carlier, D., 2018. Active tectonics around the Yakutat indentor: New geomorphological constraints on the eastern Denali, Totschunda and Duke River faults. Earth and Planetary Science Letters, vol. 482, p. 71–80, https://doi.org/10.1016/j.epsl.2017.10.051.

Massey, C., Townsend, D., Rathje, E., Allstadt, K.E., Lukovic, B., Kaneko, Y., Bradley, B., Wartman, J., Jibson, R.W., Petley, D.N., Horspool, N., Hamling, I., Carey, J., Cox, S., Davidson, J., Dellow, S., Godt, J.W., Holden, C., Jones, K., Kaiser, A., Little, M., Lyndsell, B., McColl, S., Morgenstern, R., Rengers, F.K., Rhoades, D., Rosser, B., Strong, D., Singeisen, C. and Villeneuve, M., 2018. Landslides triggered by the 14 November 2016 M_w7.8 Kaikōura earthquake, New Zealand. Bulletin of the Seismological Society of America, vol. 108, no. 3B, p. 1630–1648, https://doi.org/10.1785/0120170305.

Meighan, L.N., Cassidy, J.F., Mazzotti, S. and Pavlis, G.L., 2013. Microseismicity and tectonics of southwest Yukon Territory, Canada, using a local dense seismic array. Bulletin of the Seismological Society of America, vol. 103, no. 6, p. 3341–3346, https://doi.org/10.1785/0120130068.

Miller, D.J., 1960. The Alaska earthquake of July 10, 1958: Giant wave in Lituya Bay. Bulletin of the Seismological Society of America, vol. 50, no. 2, p. 253–266, https://doi.org/10.1785/BSSA0500020253.

Natural Resources Canada, 2025. Community internet intensity map. Earthquakes Canada, https://www.earthquakescanada.nrcan.gc.ca/recent/2025/20251206.2041/dyfi-en.php, [accessed 08/01/2026].

Nowicki Jessee, M.A., Hamburger, M.W., Allstadt, K., Wald, D.J., Robeson, S.M., Tanyas, H., Hearne, M. and Thompson, E.M., 2018. A global empirical model for near-real-time assessment of seismically induced landslides. Journal of Geophysical Research: Earth Surface, vol. 123, no. 8, p. 1835–1859, https://doi.org/10.1029/2017JF004494.

Pavlis, G.L., Bauer, M.A., Elliott, J.L., Koons, P., Pavlis, T.L., Ruppert, N., Ward, K.M. and Worthington, L.L., 2019. A unified three-dimensional model of the lithospheric structure at the subduction corner in southeast Alaska: Summary results from STEEP. Geosphere, vol. 15, no. 2, p. 382–406, https://doi.org/10.1130/GES01488.1.

Plafker, G., 1987. Regional geology and petroleum potential of the northern Gulf of Alaska continental margin. *In:* Geology and resource potential of the continental margin of western north America and adjacent ocean basins—Beaufort Sea to Baja California, p. 229–268.

Porter, C., Howat, I., Noh, M-J., Husby, E., Khuvius, S., Danish, E., Tomko, K., Gardiner, J., Negrete, A., Yadav, B., Klassen, J., Kelleher, C., Cloutier, M., Bakker, J., Enos, J., Arnold, G., Bauer, G. and Morin, P., 2023. ArcticDEM—Mosaics, Version 4.1, Harvard Dataverse, V1, https://doi.org/10.7910/DVN/3VDC4W [accessed 10/31/2025].

Read, C., Lyons, J., Stephani, E.A. and Staley, D.M., 2025. Oblique aerial photography and videography of the August 10, 2025 Tracy Arm landslide and tsunami, southeast Alaska, US Geological Survey, data release, https://www.usgs.gov/data/oblique-aerial-photography-and-videography-august-10-2025-tracy-arm-landslide-and-tsunami.

Richter, D.H. and Matson, N.A., Jr., 1971. Quaternary faulting in the eastern Alaska Range. Geological Society of America Bulletin, vol. 82, no. 6, p. 1529–1540.

Rodrıguez, C.E., Bommer, J.J. and Chandler, R.J., 1999. Earthquake-induced landslides: 1980–1997. Soil Dynamics and Earthquake Engineering, vol. 18, no. 5, p. 325–346, https://doi.org/10.1016/S0267-7261(99)00012-3.

Rubin, A.M., Gillard, D. and Got, J.-L., 1999. Streaks of microearthquakes along creeping faults. Nature, vol. 400, no. 6745, p. 635–641, https://doi.org/10.1038/23196.

Scarabello, L., Abdollahzadeh, M., Becker, J. and Pickle, R., 2025. Swiss-seismological-service/scrtdd: v1.8.9. Zenodo, https://doi.org/10.5281/zenodo.16797309.

Schaeffer, A.J., Gosselin, J.M., Audet, P., Cassidy, J.F. and Paul, C., 2026 (*this volume*). Current tectonics of the Richardson Mountains, northwestern Canada, from preliminary double-difference earthquake relocations. *In:* Yukon Exploration and Geology 2025, A. Stuart, L.H. Weston and S.K. Schultz (eds.), Yukon Geological Survey, Government of Yukon, p. 149–165.

Sethanant, I., Nissen, E., Pousse-Beltran, L., Bergman, E. and Pierce, I., 2023. The 2020 M_w6.5 Monte Cristo Range, Nevada, earthquake: Anatomy of a crossing-fault rupture through a region of highly distributed deformation. Bulletin of the Seismological Society of America, vol. 113, no. 3, p. 948–975, https://doi.org/10.1785/0120220166.

Sosio, R., Crosta, G.B., Chen, J.H. and Hungr, O., 2012. Modelling rock avalanche propagation onto glaciers. Quaternary Science Reviews, vol. 47, p. 23–40, https://doi.org/10.1016/j.quascirev.2012.05.010.

Stethem, C., Jamieson, B., Schaerer, P., Liverman, D., Germain, D. and Walker, S., 2003. Snow avalanche hazard in Canada—A review. Natural Hazards, vol. 28, p. 487–515, https://doi.org/10.1023/A:1022998512227.

US Geological Survey, 2025a. Advanced National Seismic System Comprehensive Earthquake Catalog, https://earthquake.usgs.gov/earthquakes, [accessed 08/01/2026].

US Geological Survey, 2025b. M 7.0 – 2025 Hubbard Glacier Earthquake Event Page, https://earthquake.usgs.gov/earthquakes/eventpage/us6000rsy1/executive [accessed 08/01/2026].

US Geological Survey, 2026. Quaternary fault and fold database for the United States. US Geological Survey, https://doi.org/10.5066/F7S75FJM [accessed 08/01/2026].

Utsu, T., Ogata, Y. and Matsu'ura, R.S., 1995. The Centenary of the Omori Formula for a Decay Law of Aftershock Activity. Journal of Physics of the Earth, vol. 43, no. 1, p. 1–33, https://doi.org/10.4294/jpe1952.43.1.

Velasco, A.A., Ammon, C.J., Farrell, J. and Pankow, K., 2004. Rupture directivity of the 3 November 2002 Denali fault earthquake determined from surface waves. Bulletin of the Seismological Society of America, vol. 94, no. 6B, p. S293–S299, https://doi.org/10.1785/0120040624.

Waldhauser, F. and Ellsworth, W.L., 2000. A double-difference earthquake location algorithm: Method and application to the northern Hayward fault, California. Bulletin of the Seismological Society of America, vol. 90, no. 6, p. 1353–1368, https://doi.org/10.1785/0120000006.

Waldhauser, F., 2001. hypoDD: A computer program to compute double-difference earthquake locations. Open-File Report 2001-113, US Geological Survey, https://doi.org/10.3133/ofr01113.

Wells, D.L. and Coppersmith, K.J., 1994. New empirical relationships among magnitude, rupture length, rupture width, rupture area, and surface displacement. Bulletin of the Seismological Society of America, vol. 84, no. 4, p. 974–1002, https://www.resolutionmineeis.us/sites/default/files/references/wells-coppersmith-1994.pdf.

Whelan, N., 2022. Geochronology of landslides in the Kluane Lake region, southwest Yukon. MSc thesis, Simon Fraser University. British Columbia, Canada, 165 p. plus appendices.

Yukon Geological Survey, 2021. Major Faults. Government of Yukon, https://open.yukon.ca/data/major-faults.